Optics Letters

Electrically pumped 1.5 μm InP-based quantum dot microring lasers directly grown on (001) Si

Si Zhu, Bei Shi, [iD] and Kei May Lau* [iD]

Department of Electronic and Computer Engineering, Hong Kong University of Science and Technology, Clear Water Bay, Kowloon, Hong Kong, China
*Corresponding author: eekmlau@ust.hk

Directly grown quantum dot (QD) lasers on silicon are appealing for monolithic integration of photonic circuits from a technoeconomic perspective. In this Letter, we report miniaturization of these Si-based lasers employing high-quality whispering-gallery mode microresonators. Based on previously developed InAs/InAlGaAs QDs on the complementary metal–oxide–semiconductor-standard (001) Si platform and optimized device implementation techniques, on-chip electrically pumped InP-based QD microring lasers (MRLs) on Si are successfully realized for the first time. Room-temperature pulsed lasing in the 1.5 μm wavelength band, with a threshold of 50 mA, is measured for 50-μm-diameter MRLs. Lasing up to 70°C is achieved with a characteristic temperature of 51.5 K. © 2019 Optical Society of America

The past decades have witnessed the booming development of silicon photonic integrated circuits (PICs) for their promise in complementary metal–oxide–semiconductor (CMOS)-compatible production and monolithic integration with microelectronics [1]. To enable a low-cost and robust approach for integrating Si-based light sources in the longer term, efforts have been devoted to direct epitaxy of III-V lasers on Si [2], among which, an InP-based material system remains the primary choice for practical on-chip lasers in telecommunication wavelengths, due to a broadband coverage for III-V alloys lattice-matched to InP [3] and the mature techniques in active/passive integration for InP-based PICs [4–6]. Recent successful demonstrations of lasers directly grown on Si utilizing other material systems and quantum dots have gained traction for this approach [7–16]. Meanwhile, miniaturizing the footprints of these Si-based lasers while maintaining the electrically pumped configuration is of great necessity for practical low-power consumption and high-speed dense optical interconnects. Self-assembled quantum dots (QDs), as emerging superior gain elements, offer unique characteristics of strong carrier localization in discrete three-dimensional nanostructures and less sensitivity to surface defects. Benefiting from this, incorporating QDs promises a greater immunity to defects in III-V/Si heteroepitaxy, and suppresses the severe spreading

and surface recombination of nonequilibrium carriers in ultrasmall lasers, leading to good device performance with a low threshold and high temperature stability.

Whispering-gallery mode (WGM) microlasers hold great potential for dense photonic integration. Previously we have demonstrated the first C-band QD microdisk lasers grown on Si with diameters of 1.5 and 4 μm by photon pumping [17,18]. In this Letter, we report the first demonstration of electrically pumped microring lasers (MRLs) grown and fabricated on Si emitting at the 1.5 μm wavelength band. On the basis of our recently reported InP-based QD laser on Si structure [19], 50-μm-diameter MRLs with deep-mesa geometry have been designed and fabricated, achieving lasing up to 70°C under pulsed current injection. The effects of the etching depth below the planar active core and the resonator radius are discussed. And temperature-dependent characteristics are also studied.

The epitaxial structure for a QD laser on (001) Si is shown in Fig. 1(a), which is identical to what we have reported in [19]. The 2-μm-thick GaAs buffer consisting of 15 periods of $Al_{0.3}Ga_{0.7}As$/GaAs superlattices (SLs) grown on V-grooved (001) Si resulted in a smooth and antiphase boundary (APB)-free growth front. Three cycles of thermal cycle
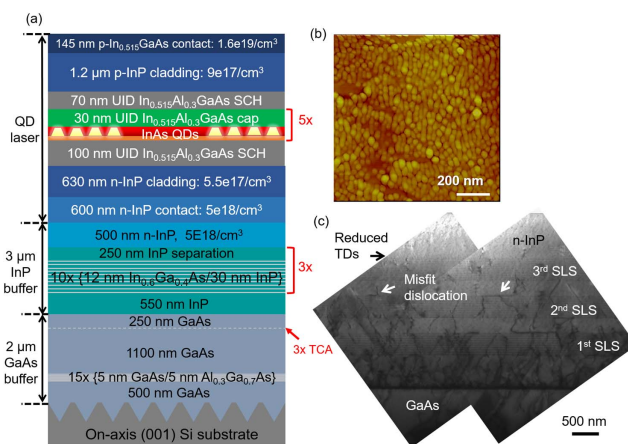

Fig. 1. (a) Epitaxial structure diagram of the 1.5 μm QD laser on (001) Si; (b) AFM image of the InAs/InAlGaAs QDs on Si; (c) cross-sectional TEM image of the InGaAs/InP SLS inserted in the InP buffer, showing an apparent dislocation filtering effect.

annealing (TCA) effectively reduced the threading dislocation (TD) densities further in the GaAs buffer [20]. In the subsequent InP buffer growth, three sets of 10-period $In_{0.6}Ga_{0.4}As$/InP strain layer superlattices (SLSs) were inserted to further facilitate the annihilation of TDs [Fig. 1(c)]. The topmost 500 nm InP buffer was Si-doped to serve as the n-contact layer, leading to a total InP buffer thickness around 3 μm. The QD laser structure includes a 145 nm InGaAs p-contact layer, a 1.2 μm p-InP upper cladding, a 332 nm active core comprising five stacks of InAs/InAlGaAs QDs and InAlGaAs separate confined heterostructures (SCHs), a 630 nm n-InP cladding, and a 600 nm n-InP contact layer, as seen in Fig. 1(a). No cracks were identified on the final surface. Together with a 500 nm n-InP buffer, the effective lower cladding thickness can vary from 630 nm to 1.7 μm according to the actual etching depth below the active core. The confinement factor (Γ) in the InAs QDs is calculated to be ∼1.6% in this laser structure. The coherent multistack QDs on Si, characterized by atomic force microscopy (AFM) in the inset of Fig. 1(b), present a QD density of 4.5×10^{10} cm^{-2}. Cross-sectional TEM image of the embedded multiple stack of QDs can be found in [21]. And, the established five-stack InAs/InAlGaAs QDs in the active core exhibit a photoluminescence (PL) spectrum centered around 1.51 μm [19].

Different from conventional semiconductor lasers using shallow-etched ridge waveguides, ring lasers with a ring radius below 100–150 μm suffer from rapidly increasing bending loss [22]. Therefore, smaller devices generally require a deeply etched profile well through the active core. This facilitates a much greater optical confinement at the expense of other adverse effects, including enhanced surface recombination of carriers and optical scattering losses due to fabrication deficiencies. Nevertheless, three-dimensional carrier confinement of QDs helps prevent their diffusion towards nonradiative recombination centers, which mitigate the problems associated with sidewall imperfections and defects.

To investigate the influences of the deep-etching depth and ring radius, simulation analysis has been performed to study the radiation loss of the microring resonator based on the QD laser on Si structure described above. Figures 2(a) and 2(b) present the sectional mode profile of the fundamental WGM with different effective lower cladding thicknesses of 1.2 μm and 3 μm, resulting in total deep-etching depths of 2.9 μm and 4.7 μm, respectively. Only the TE-polarized mode was taken into account here because the compressive strained InAs/InAlGaAs QDs provide higher gain for TE mode than TM mode [23]. It is clearly seen that the bending loss/substrate leakage is more severe for a shallower etched ring resonator. In the simulation, we did not include possibly significant scattering losses that may have resulted from defects or roughness from fabrication imperfection.

Figure 2(c) presents the radiation loss (α) as a function of lower cladding thickness. The α values were determined from the simulated intrinsic Q factors according to the formula $Q = \frac{2\pi f_0}{\alpha v_g}$, in which f_0 is the Eigen resonant frequency of the calculated WGM and v_g is the group velocity. It is obvious that the etching depth has a huge influence on the radiation loss, which exponentially increases to 15 cm^{-1} when the thickness of the etched lower InP cladding was reduced to 1.2 μm. With the lower cladding thickness fixed at 2 μm,
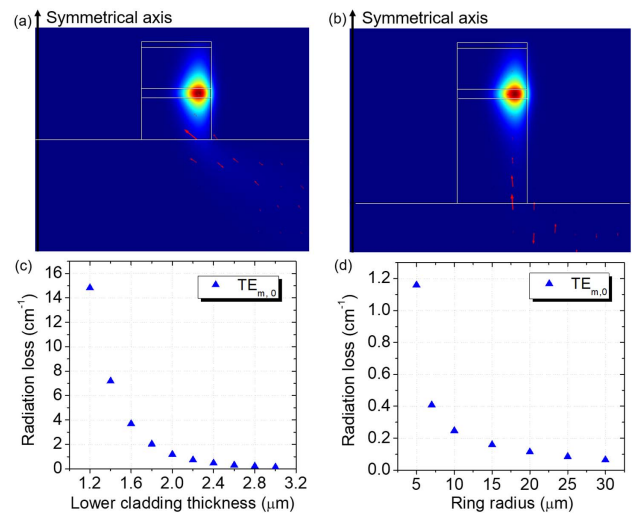

Fig. 2. Cross-sectional mode profile of the fundamental TE mode in a 6-μm-radius microring resonator with (a) 1.2 μm and (b) 3 μm etching depth below the active core. Radiation loss of the fundamental TE mode as a function of (c) lower cladding thickness and (d) ring radius.

an exponential relationship between α and microring radius is also calculated in Fig. 2(d). Based on the results of QD FP lasers on Si using the identical epi-structure [19], the minimum FP cavity length that supported lasing was 1 mm, corresponding to a mirror loss on the order of 10^1 cm^{-1}. Therefore, a microring resonator designed to have a radiation loss less than 10^1 cm^{-1} would have a higher chance to lase.

With the above considerations in mind, device fabrication was carried out following the processes depicted in Fig. 3. Ring waveguides were first patterned and transferred to a 700 nm SiO_2 hard mask by dry etching based on C_4F_8/He/H_2 gas mixture. Then the ring mesa was etched by 3.2 μm in depth into the epi-layers using inductively coupled plasma (ICP) etching, with around 200 nm n-InP (Si doped, 5×10^{18}/cm^3) remaining for contact. The requirements for the dry etching steps are especially stringent for the strongly lateral confined microring resonators. The sidewall smoothness is critical in determining the device performance. Besides, instead of forming the n-contact at the backside of the wafer, which is more straightforward, a top–top contact geometry adopted here prevents the current injection through the defective III-V/Si interface. Therefore, the smoothness of the etched n-InP bottom surface is equally crucial to form a good ohmic contact at the front side. Thus, optimization of the deep etching conditions is needed.
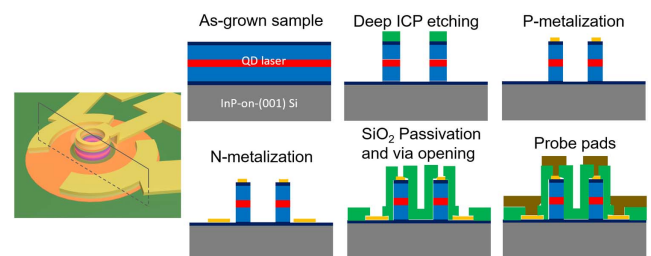

Fig. 3. Process steps of the QD microring lasers on Si, presented in a sliced sectional view.

Chlorine-based reactive etchants are often adopted for a fast deep etch of InP-based materials. However, the byproduct $InCl_x$ has very low volatility that will redeposit, resulting in a grassy etched surface, known as the micromasking effect [24]. Hence, the ICP chamber is usually heated to 200°C or higher to assist the volatilization of $InCl_x$ [25,26]. However, it is not always practical to perform etching at such an elevated temperature. Here we have developed the ICP etching process performed at room temperature, taking advantage of the sample self-heating during the physical and chemical reactions. The gas mixture chosen includes a reactive gas (BCl_3), an inert bombardment gas (Ar), and an additional surface passivation gas (N_2). The gas ratio ($BCl_3 : Ar : N_2 = 6:10:2$ sccm), ICP coil/platen power (750 W/100 W), and chamber pressure (4 mTorr) are the key parameters determined in the optimization. 70° tilted SEM images shown in Figs. 4(a) and 4(b) compare the difference between deep-etched morphologies before and after optimization of the room-temperature ICP process. A remarkable improvement in the bottom surface smoothness is demonstrated.

After deep ICP etching, Ti/Pt/Au and Ge/Au/Ni/Au were deposited for the *p* and *n* contact metals. Subsequently, rapid thermal annealing (RTA) was performed at 400°C for 2 min for a better metal–semiconductor contact. 800 nm PECVD SiO_2 was grown for passivation, on which the p- and n-via were then opened. Finally, 1 μm Ti/Al probe pads were deposited by sputtering. Figure 4(c) presents the top-down SEM image of an as-fabricated MRL with an outer radius of 25 μm and a waveguide width of 7 μm.

For room-temperature light-current-voltage (L-I-V) measurements, the device under test (DUT) was placed on a copper stage with the thermoelectric cooler (TEC) set at 20°C. Figure 5(a) shows the voltage-current (V-I) characteristic of
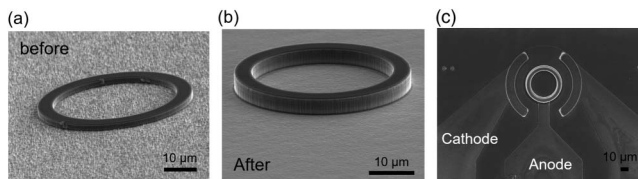
one laser with a 25 μm outside radius and 7 μm waveguide width under continuous-wave current injection. Good electrical contacts formation for the microlaser is indicated by a typical V-I property for a P-I-N diode with a turn-on voltage of 0.7 V and a series resistance of 10 Ω. Figure 5(b) presents the light-current (L-I) curve of the MRL. To effectively measure the output power, we used an integrating sphere with an InGaAs detector placed side by side near the DUT for scattered output collection. The DUT was subjected to continuous injections of current pulses of 400 ns duration every 80 μs from a pulsed current source. The threshold extracted around 50 mA is comparable with other reported 1.55 μm QD MRLs grown on native InP substrates [27], which operate in a continuous-wave condition. The corresponding threshold current density of 5.3 kA/cm^2 is higher than that of the 1.5 μm QD FP lasers on Si we reported (1.6–3 kA/cm^2 for 5–1 mm long lasers) [19], which is ascribed to the increased radiation loss in the ring resonator compared to the mirror loss of the FP cavity, and higher scattering loss as the WGMs are confined close to the resonator sidewall.

Figure 6 displays a set of lasing spectra under progressively increased pulsed pumping currents. The primary lasing WGM appeared at 1510 nm, and multimode lasing of adjacent WGMs is observed at elevated injection currents. Meanwhile, the dominant lasing peak hopped to modes at longer wavelength due to the redshift of the gain spectrum. The free-spectrum range (FSR) of the fundamental TE-polarized WGMs obtained from the spectrum is ~4 nm. The group index can then be calculated to be $n_g = 3.718$ from FSR $= \frac{\lambda^2}{2\pi n_g R_0}$, in which R_0 is the radius of the modal core and simulated to be 24.4 μm. The background gray curve shows the QDs' spontaneous emission obtained from the electroluminescence of the test structure. Lasing WGMs of the microring all appeared at the lower energy side of the broadband QD emission, which is attributed to the reabsorption of the high-energy photons and a stronger capture efficiency of larger QDs.

Temperature characteristics of the device were also measured. Figure 7(a) presents the L-I characteristics of a 25-μm-radius device with a stage temperature ranging from 20°C to 70°C. Lasing behavior sustains up to 70°C. The capability of high-temperature operations promises their potential applications in Si-based optoelectronic chips. The relationship of the

Fig. 4. 70° tilted view of the ring resonator (a) before and (b) after the optimization of room-temperature deep ICP process. (c) Top view SEM images of the microring laser with an outer radius of 25 μm and waveguide width of 7 μm.
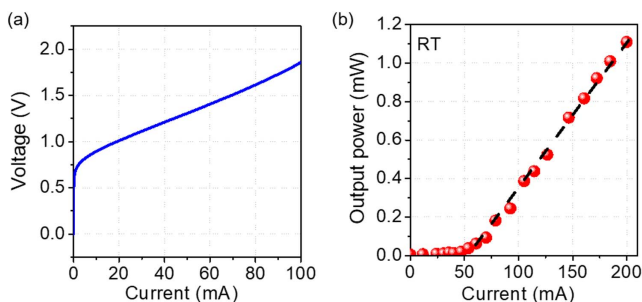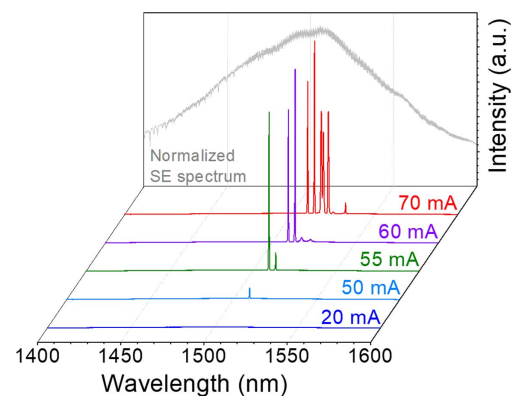

Fig. 5. (a) V-I and (b) L-I characteristics of the QD MRL on Si with an outer radius of 25 μm and waveguide width of 7 μm.

Fig. 6. Lasing spectra at various current injection levels. The background gray curve reflects the normalized spontaneous emission spectrum.
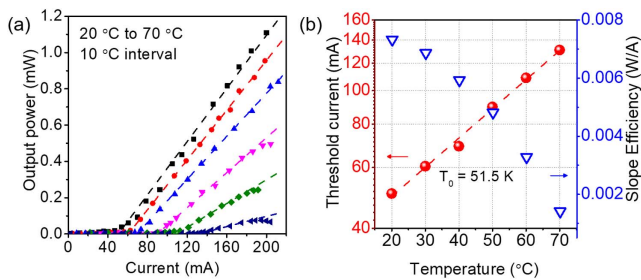
Fig. 7. (a) L-I curves at different temperatures; (b) threshold current and slope efficiency change as a function of temperature. The characteristic temperature T_0 was extracted to be 51.5 K.

threshold current and the slope efficiency as a function of temperature is shown in Fig. 7(b). It is noted that the slope efficiency is degrading accordingly with the temperature increment. Simple fitting of the data resulted in a characteristic temperature of 51.5 K, which agrees with the value we have reported in [20] for 1.5 µm QD FP lasers on Si (58.7 K).

In summary, we have presented the successful realization of the first 1.5 µm band QD MRL monolithically grown on CMOS-compatible (001) Si substrate. Influential structural parameters such as a lower cladding thickness and microring radius have been studied for cavity loss management. Deeply etched microring resonators with front-side contact geometry have been designed and fabricated. In order to achieve both smooth sidewall and etched surfaces, a deep ICP etching process performed at room temperature has been developed. Electrically pumped pulsed laser emissions in a microring resonator 50 µm in diameter have been achieved, with a room-temperature threshold around 50 mA. We have also demonstrated the capability of these QD microlasers on Si operating at elevated temperatures up to 70°C. All these results substantiate the possibility of realizing versatile active photonic devices on Si with more stringent requirements. Further miniaturizing the device size would require a thicker lower cladding, to compensate for the exponentially increased radiation loss introduced by the radius shrinkage. To improve the device performance such as lower thresholds and continuous-wave lasing, enhancing the optical quality of the InAs QDs as well as reducing the defect density of the InP-on-Si templates are first priorities. Meanwhile, further lowering the series resistance by introducing n-type doping in the entire III-V buffer layers and integrated heatsink designs would help manage the prominent self-heating in microlasers, which could also contribute to better performance.

REFERENCES

1. A. H. Atabaki, S. Moazeni, F. Pavanello, H. Gevorgyan, J. Notaros, L. Alloatti, M. T. Wade, C. Sun, S. A. Kruger, H. Meng, K. A. Qubaisi, I. Wang, B. Zhang, A. Khilo, C. V. Baiocco, M. A. Popović, V. M. Stojanović, and R. J. Ram, Nature **556**, 349 (2018).
2. Z. Zhou, B. Yin, and J. Michel, Light Sci. Appl. **4**, e358 (2015).
3. S. Bhowmick, M. Z. Baten, T. Frost, B. S. Ooi, and P. Bhattacharya, IEEE J. Quantum Electron. **50**, 7 (2013).
4. L. A. Coldren, S. C. Nicholes, L. Johansson, S. Ristic, R. S. Guzzon, E. J. Norberg, and U. Krishnamachari, J. Lightwave Technol. **29**, 554 (2011).
5. L. M. Augustin, R. Santos, E. Haan, S. Klejin, P. J. A. Thijs, S. Latkowski, D. Zhao, W. Yao, J. Bolk, H. Ambrosius, S. Mingaleev, A. Richter, A. Bakker, and T. Korthorst, IEEE J. Sel. Top. Quantum Electron. **24**, 6100210 (2018).
6. J. Klamkin, H. Zhao, B. Song, Y. Liu, B. Isaac, S. Pinna, F. Sang, and L. Coldren, in *IEEE BiCMOS and Compound Semiconductor Integrated Circuits and Technology Symposium* (2018), p. 8.
7. Y. Wang, S. Chen, Y. Yu, L. Zhou, L. Liu, C. Yang, M. Liao, M. Tang, Z. Liu, J. Wu, W. Li, I. Ross, A. J. Seeds, H. Liu, and S. Yu, Optica **5**, 528 (2018).
8. Y. Wan, J. Norman, Q. Li, M. J. Kennedy, D. Liang, C. Zhang, D. Huang, Z. Zhang, A. Y. Liu, A. Torres, D. Jung, A. C. Gossard, E. L. Hu, K. M. Lau, and J. E. Bowers, Optica **4**, 940 (2017).
9. N. Kryzhanovskaya, E. Moiseev, Y. Polubavkina, M. Maximov, M. Kulagina, S. Troshkov, Y. Zadiranov, Y. Guseva, A. Lipovskii, M. Tang, M. Liao, J. Wu, S. Chen, H. Liu, and A. Zhukov, Opt. Lett. **42**, 3319 (2017).
10. S. Chen, W. Li, J. Wu, Q. Jiang, M. Tang, S. Shutts, S. N. Elliott, A. Sobiesierski, A. J. Seeds, I. Ross, P. M. Smowton, and H. Liu, Nat. Photonics **10**, 307 (2016).
11. A. Castellano, L. Cerutti, J. B. Rodriguez, G. Narcy, A. Garreau, F. Lelarge, and E. Tournié, APL Photon. **2**, 061301 (2017).
12. A. Y. Liu, J. Peters, X. Huang, D. Jung, J. Norman, M. L. Lee, A. C. Gossard, and J. E. Bowers, Opt. Lett. **42**, 338 (2017).
13. A. Hazari, F. C. Hsiao, L. Yan, J. Heo, J. M. Millunchick, J. M. Dallesasse, and P. Bhattacharya, IEEE J. Quantum Electron. **53**, 6300109 (2017).
14. J. Kwoen, B. Jang, J. Lee, T. Kageyama, K. Watanabe, and Y. Arakawa, Opt. Express **26**, 11568 (2018).
15. J. Yang and P. Bhattacharya, Opt. Express **16**, 5136 (2008).
16. R. E. Camacho-Aguilera, Y. Cai, N. Patel, J. T. Bessette, M. Romagnoli, L. C. Kimerling, and J. Michel, Opt. Express **20**, 11316 (2012).
17. S. Zhu, B. Shi, Q. Li, Y. Wan, and K. M. Lau, Opt. Express **25**, 31281 (2017).
18. B. Shi, S. Zhu, Q. Li, C. W. Tang, Y. Wan, E. L. Hu, and K. M. Lau, Appl. Phys. Lett. **110**, 121109 (2017).
19. S. Zhu, B. Shi, Q. Li, and K. M. Lau, Appl. Phys. Lett. **113**, 221103 (2018).
20. M. Yamaguchi, A. Yamamoto, M. Tachikawa, Y. Itoh, and M. Sugo, Appl. Phys. Lett. **53**, 2293 (1988).
21. B. Shi, Y. Han, Q. Li, and K. M. Lau, IEEE J. Sel. Top. Quantum Electron. **25**, 1900711 (2019).
22. G. Mezosi and M. Sorel, *Compact Semiconductor Lasers* (Wiley-VCH, 2014), Chap. 6.
23. N. Yasuoka, K. Kawaguchi, H. Ebe, T. Akiyama, M. Ekawa, K. Morito, M. Sugawara, and Y. Arakawa, IEEE Photon. Technol. Lett. **20**, 1908 (2008).
24. M. Vernon, T. Hayes, and V. Donnelly, J. Vac. Sci. Technol. A **10**, 3499 (1992).
25. C. Carlström, R. van der Heijden, F. Karouta, R. W. van der Heijden, and H. W. M. Salemink, J. Vac. Sci. Technol. B **24**, L6 (2006).
26. S. L. Rommel, J. H. Jang, W. Lu, G. Cueva, L. Zhou, and I. Adesida, J. Vac. Sci. Technol. B **20**, 1327 (2002).
27. Y. Barbarin, S. Anantathanasarn, E. A. J. M. Bente, Y. S. Oei, M. K. Smit, and R. Notzel, IEEE Photon. Technol. Lett. **18**, 2644 (2006).